bioRxiv preprint doi: https://doi.org/10.1101/441014; this version posted October 12, 2018. The copyright holder for this preprint (which was not certified by peer review) is the author/funder. All rights reserved. No reuse allowed without permission.

Segregated encoding of spatiotemporal features in the mouse visual cortex

Xu Han[1,2], Ben Vermaercke[1,2,3], Vincent Bonin[1,2,3,4]

[1]Neuro-Electronics Research Flanders, Kapeldreef 75, 3001 Leuven, Belgium.
[2]Department of Biology & Leuven Brain Institute, KU Leuven, 3000 Leuven, Belgium.
[3]VIB, 3001 Leuven, Belgium.
[4]imec, 3001 Leuven, Belgium.

Correspondence should be addressed to V.B. (email: vincent.bonin@nerf.be).

Abstract

Understanding visual processing requires a detailed description of computations performed by neurons across stages of the visual system. However, the diverse tunings of neurons beyond the primary visual cortex (V1) have yet to be fully characterized. Using two-photon calcium imaging and stochastic visual stimuli, we catalogued the response properties of a dense sample of 40,000 neurons in V1 and six secondary visual areas of awake mice. All areas encode unique sets of features with distinct spatiotemporal preferences, motion speed selectivity, and differential responses to oriented and non-oriented stimuli. Central areas V1 and LM have the most diverse tunings, with distributed spatiotemporal preferences and a moderate bias for non-oriented stimuli. Preferences of V1 and LM neurons differ strikingly showing tuning to low and midrange spatiotemporal frequencies, respectively. Lateral areas PM and LI are highly biased towards high spatial and low temporal frequencies, showing weak selectivity for motion speed. Anterior areas AL, RL and AM are highly biased towards high temporal frequencies and have the largest proportion of motion tuned cells. Accordingly, activity patterns in these areas carry more information about motion speed than any other visual areas. With regards to spatial preferences, LI differs strikingly from PM and anterior areas in that it is heavily biased towards non-oriented stimuli. The data provides a detailed description of the segregation of encoding of spatiotemporal feature in the rodent visual cortex and provides a stark demonstration of the high functional specialization of visual areas.

Introduction

Recent studies on mice harvested important insights of the neural basis underpinning sensory computations. On the one hand, the genetic and experimental access to the mouse visual system revealed fundamental organizations at multiple stages of visual processing (Maruoka et

bioRxiv preprint doi: https://doi.org/10.1101/441014; this version posted October 12, 2018. The copyright holder for this preprint (which was not certified by peer review) is the author/funder. All rights reserved. No reuse allowed without permission.

al., 2017; Wanner et al., 2017; Han et al., 2018; Liang et al., 2018) and specific circuitries underlying a range of computations (Ko et al., 2011, 2013, Lien and Scanziani, 2013, 2018; Reinhold et al., 2015). In parallel, studies of mouse visual behaviors have revealed a greater richness than previously recognized. Mouse are able to identify arbitrary shapes and pictures (Brigman et al., 2005; Nithianantharajah et al., 2013), differentiate coherent motion direction (Stirman et al., 2016; Marques et al., 2018), using visual cues to navigate (Prusky et al., 2000; Harvey et al., 2009; Chen et al., 2013) or guide accurate approach to the prey (Hoy et al., 2016), and associate stimulus identity with stimulus value (Poort et al., 2015; Burgess et al., 2016). Many of these complex visual behaviors rely on an elaborate neural network of higher-order visual cortical areas. Therefore, a necessary step to understand the neural basis for those visual behaviors is to understand how specific visual stimuli are encoded in the higher visual cortex.

The mouse visual cortex encompasses over ten retinotopic higher visual areas surrounding V1 (Wang and Burkhalter, 2011; Garrett et al., 2014; Zhuang et al., 2017). These areas are suggested to be specialized for specific visual features. Surveys in anesthetized mice found neurons in higher visual areas respond to drifting gratings with distinct spatiotemporal frequencies and speeds, and pattern versus component motion (Marshel et al., 2011; Roth et al., 2012; Tohmi et al., 2014; Juavinett and Callaway, 2015; Smith et al., 2017). However these stimulus preferences might be very different in the awake brain since anesthesia profoundly affects visual responses (Haider et al., 2013; Lien and Scanziani, 2013; Aasebø et al., 2017). Nevertheless, there have been far fewer studies of the response properties of neurons in higher visual areas in awake mice, and these have only focused on a small set of areas (Andermann et al., 2011; Glickfeld et al., 2013).

To understand how specific visual features are encoded in the visual cortex, we undertook a comprehensive functional characterization of layer 2/3 neurons in V1 and six higher visual areas in awake mice using two-photon calcium imaging. Using a library of stochastic visual stimuli (spectral noise stimuli), we found neurons in distinct higher visual areas present distinct selectivities for the spatiotemporal frequency, visual motion speed and spatial stimulus anisotropy (oriented versus non-oriented stimuli). Population coding analysis further revealed greater speed discriminability in higher visual areas than V1. Overall, higher visual areas present segregated encoding of spatiotemporal features that might underpin distinct computations, such as processing of visual motion and shape.

bioRxiv preprint doi: https://doi.org/10.1101/441014; this version posted October 12, 2018. The copyright holder for this preprint (which was not certified by peer review) is the author/funder. All rights reserved. No reuse allowed without permission.

Results

Cortical neurons are highly selective for spectral noise stimuli

Using two-photon calcium imaging, we recorded cellular responses to spectral noise stimuli in layer 2/3 of V1 and six higher visual areas (LM: lateromedial; AL: anterolateral; RL: rostrolateral; AM: anteromedial; PM: posteromedial; LI: laterointermediate; Figure 1A – figure supplement 1) in awake Thy1-GCaMP6s mice (Figure 1B; Dana et al., 2014).

The spectral noise stimuli consisted of 4s-epochs of spatiotemporally filtered bandpass noise stimuli interleaved by 4s-epochs of equiluminent gray screen (Figure supplement 2; Materials and Methods). The stimuli spanned a broad range of spatial (0.02 to 0.32 cycle per degree) and temporal frequencies (0.5 to 16 Hz) as well as various degrees of orientation bandwidth (5, 10, 40 degree, and no filter for non-oriented stimuli). These stimuli were designed to drive diverse orientation-tuned neurons. At one extreme, ISO stimuli had isotropic spatial frequency spectra with uniform power in all orientations, resembling a cloud of moving dots (Figure 1C -- figure supplement 2A). At the other, ANISO stimuli (Figure 1C – figure supplement 2A) had energy within a narrow orientation band (5 degree), resembling sinusoidal gratings. A global rotation was implemented in ANISO stimuli to sweep the entire orientation space within each stimulus epoch.

In V1, around 80% of fluorescent neurons were responsive to at least one stimulus condition; this number is lower in higher visual areas (40~65%, Figure supplement 3B). In addition, V1 neurons responded more reliably than those in higher visual areas (trial-to-trial correlation: V1 vs others, KS tests with Bonferroni correction, all p values < 0.01; Figure supplement 3C). These data demonstrate V1 neurons robustly respond to spectral noise stimuli and encode reliable visual representations, whereas neurons in higher visual areas are selective for appropriate stimulus dimensions. Neurons that didn't respond might require stimulus dimensions that were not explored in this study (visual or non-visual).

We further investigated whether ISO and ANISO stimuli activated distinct populations of neurons. We found distinct stimulus preferences across neurons. A subset of neurons (Figure 1C, example cell 1) selectively responded to ISO stimuli (Figure 1D, ISO), showing a strong preference for non-oriented stimuli; whereas another (Figure 1C, cell 2) solely responded to ANISO stimuli (Figure 1D, ANISO), preferring oriented stimuli. Each subset comprised a substantial fraction of the responsive neurons in all areas (Figure 1E, ~20 to 40% per area). The remaining responsive cells (Figure 1C, cell 3) responded to both ISO and ANISO stimuli with

bioRxiv preprint doi: https://doi.org/10.1101/441014; this version posted October 12, 2018. The copyright holder for this preprint (which was not certified by peer review) is the author/funder. All rights reserved. No reuse allowed without permission.

comparable response profiles, albeit the difference in the response strengths (Figure 1D, group 'Both'). This demonstrates distinct subsets of cortical neurons encode oriented or non-oriented features of the visual scene.

By characterizing the responses to spectral noise stimuli of populations of thousands of neurons in V1 and higher visual areas, we could quantitatively determine the degree to which areas in the mouse visual cortex are specialized for distinct spatiotemporal features.

Distinct population response profiles across areas

To determine whether cortical areas contain distinct functional populations, we categorized the reliably responsive neurons using a non-supervised clustering approach (spectral clustering, see Method and Materials). For each area, we obtained a subsample of 2000 neurons with random selection, each neuron yielded a vector of peak-normalized responses to ISO and ANISO stimuli (Figure 2B). We firstly tested whether there are discrete functional types or not. Response profiles of cortical neurons were highly diverse and covered the response space in a continues manner. Therefore, we didn't observe discrete functional types based on the response profiles to spectral noise stimuli (Figure supplement 4A). Nevertheless, we used the clustering approach to investigate population response profiles across areas. Neurons were categorized into 12 broad groups, showing similar response profiles within each group and remarkable differences across groups (Figure 2A -- Figure supplement 4B). These groups presented distinct response properties for spatiotemporal frequencies and stimulus anisotropy (Figure supplement 5). Each area contained a unique composition of functional groups (Figure 2B, C). The interareal difference was estimated as the Euclidian distance of population compositions between pairs of areas, shown in a hierarchical tree (Figure 2D). V1 was distinct from higher visual areas, nevertheless more similar to LM. LM showed a uniform distribution of functional groups. Anterior areas, AL, RL and AM, showed similar abundance of a set of clusters and thus form a separate branch from other areas. On the other side of the tree, PM and LI contained functional clusters nearly non-overlapping with the anterior areas. These results reveal distinct population response profiles across cortical areas, suggesting the functional segregation for the processing of distinct spatiotemporal features.

To investigate how spatiotemporal information are encoded in the visual cortex, we undertook quantitative analysis on individual spatiotemporal features within and across areas.

bioRxiv preprint doi: https://doi.org/10.1101/441014; this version posted October 12, 2018. The copyright holder for this preprint (which was not certified by peer review) is the author/funder. All rights reserved. No reuse allowed without permission.

Distinct preferences for the stimulus anisotropy across cortical areas

Cortical neurons showed diverse preferences for ISO and ANISO stimuli (Figure 1, 2B), which differed in the orientation characteristics. We then asked whether neurons were tuned for the degree of orientedness, which we refer as stimulus anisotropy. The tuning curve was measured as the responses to four degrees of anisotropy at the preferred spatial frequencies (Figure 3A, B). The stimulus anisotropy index (SAI) is the difference/sum ratio of the responses to the most anisotropic and isotropic stimuli. From -1 to 1, neurons shift the preferences from isotropic to anisotropic stimuli. The tuning of individual cells matched their response preferences for ISO or ANISO stimuli (Figure 3B; same cells in Figure 1C). Neurons selectively responding to ISO stimuli strongly responded to the non-oriented stimuli, the responses declined quickly as the stimuli became anisotropic (Cell 1; SAI = -0.91). ANISO neurons selectively responded to oriented stimuli, preferring higher degrees of anisotropy (Cell 2; SAI = 0.95). The remaining populations were broadly tuned, responding invariantly to different degrees of anisotropy (Cell 3, SAI = -0.1).

To investigate whether neurons in different areas have distinct preferences for stimulus anisotropy, we compared average tuning curves (Figure 3C) and distributions of stimulus anisotropy index across areas (Figure 3D). The average responses of V1 and LM neurons peaked at non-oriented stimuli, and decreased to increasingly oriented stimuli (Figure 3C). Likewise, the distributions of tuning index also deviated towards isotropic stimuli (Figure 3D). Areas AL, RL, AM and PM, showed heterogeneous preferences, encoding a uniform representation of the stimulus anisotropy space. Contrastingly, area LI showed a pronounced bias for non-oriented stimuli (Figure 3C, D), distinct from other areas. These results demonstrate mouse cortical areas encode distinct information of non-oriented and oriented components of the visual scene.

LM neurons encode a uniform representation of spatiotemporal frequency space

Besides the selectivity for stimulus anisotropy, cortical neurons also showed diverse responses to spatiotemporal frequencies (Figure 2B). Individual neurons' tuning curve for the spatiotemporal frequency was estimated by fitting a two-dimensional Gaussian model to the trial-averaged responses to the preferred stimuli (ISO or ANISO stimuli; Figure 4A, B; Priebe et al., 2003; Andermann et al., 2011).

We firstly compared the spatiotemporal selectivities of LM neurons with those in V1, as LM neurons were shown to have similar functional properties as V1 neurons (Van Den Bergh et al., 2010; Marshel et al., 2011). Both areas contained neurons showing highly diverse preferences

bioRxiv preprint doi: https://doi.org/10.1101/441014; this version posted October 12, 2018. The copyright holder for this preprint (which was not certified by peer review) is the author/funder. All rights reserved. No reuse allowed without permission.

for spatial and temporal frequencies, spanning the entire frequency spectra (Figure 4E, F). V1 population, however, showed the preference for lower frequencies; whereas LM population formed a uniform representation of the frequency space with a slight bias for intermediate frequencies (Figure 4C: 20 random response fits; 4E: fraction of responsive cells to certain frequencies). These differences were also evident in the distribution of preferred frequencies and the proportion of neuron of different passband properties (Figure 4D, F-- figure supplement 6).

In the spatial frequency domain, V1 preferred lower frequencies than LM (Figure 5A; median values, V1 vs LM: 0.055 vs 0.074 cpd; KS test with Bonferroni correction, $p < 0.01$), and had more lowpass cells (Figure supplement 6C; V1 vs LM: 33% vs 27%), indicating a tendency to respond to even lower spatial frequencies. Cutoff frequencies (Figure 5B) were measured to estimate the range of frequency represented by each neuronal population. V1 neurons preferentially represented low spatial frequencies (median low and high cutoffs: 0.03 and 0.137 cpd), contrasting LM neurons that preferred intermediate frequencies (median cutoffs: 0.046 and 0.163 cpd; V1 vs LM, KS-test: $p< 0.01$ for each pair). In addition, the spatial frequency tuning width of V1 bandpass cells were wider than those in LM, suggesting that LM neurons were more selective for spatial frequencies (Figure supplement 6D; KS test, $p<0.01$).

In the temporal frequency domain (Figure 5C, D -- figure supplement 6E, F), LM neurons preferred higher frequencies than V1 (higher preferred and cutoff frequencies, and less lowpass cells in LM). The bandwidths were comparable for V1 and LM neurons (V1 vs LM: 2.09 vs 2.02 octave; KS test, $p>0.05$). Altogether, these results demonstrate the spatiotemporal selectivity is different between LM and V1: LM neurons encode a uniform representation of the spatiotemporal frequency space, whereas V1 shows an overrepresented lower frequency domain.

Anterior areas prefer low spatial and high temporal frequencies

Anterior areas, including AL, RL and AM, preferentially responded to low spatial and high temporal frequencies (Figure 4,5 – figure supplement 6). Among all areas, RL showed the utmost preference for low spatial and high temporal frequencies (median preferred frequencies: 0.062 cpd and 4.59 Hz; KS test: $p < 0.01$ for all area pairs). It contained the largest fraction of spatially lowpass / temporally highpass cells among all areas (25% vs 1~15%). In comparison, AM neurons were biased to intermediate frequencies (median preferred frequencies: 0.085 cpd and 3.34 Hz) and contained a substantial group of spatially bandpass neurons (64%). AL showed median preferred frequencies comparable to AM, but higher diversities in the population

bioRxiv preprint doi: https://doi.org/10.1101/441014; this version posted October 12, 2018. The copyright holder for this preprint (which was not certified by peer review) is the author/funder. All rights reserved. No reuse allowed without permission.

(Figure 4F), resulting in a more uniform representation of low to intermediate spatial frequencies (Figure 4E). These results demonstrate overall similar preferences for low spatial, high temporal frequencies in anterior areas, suggesting the specialization for encoding fast-changing, large-scale stimuli.

Lateral areas prefer high spatial and low temporal frequencies

In contrast to anterior areas, areas LI and PM (Figure4,5—figure supplement 6), who are situated at lateral sides of the visual cortex, preferred high spatial and low temporal frequencies (median preferred, PM vs LI: 0.158 vs 0.142 cpd; 1.29 vs 1.36 Hz; KS test, for each pair, $p<0.05$). PM and LI contained different subpopulations of neurons (Figure 5A). PM population presented a bimodal distribution in the spatial frequency domain with a small and a large fraction of neurons responding to low and high frequencies, respectively; whereas LI contained more diverse population that responded to a broader range of spectrum deviated to higher spatial frequencies. Nevertheless, PM and LI presented overall similar preferences for slow-moving, refined stimuli, opposing to anterior areas.

Preferences shifted to higher frequencies in awake mice

We compared our results to Marshel et al., 2011, where the same set of areas were investigated in anesthetized mice. Individual areas' preferred frequencies in the current study are remarkably higher (up to 2-fold) than in Marshel's study (Figure 5E, F). By contrast, our results are largely comparable to the observation in awake mice (in comparison to Andermann et al., 2011; except TF tuning for V1). These comparisons might reflect the influence of different brain states on the neural representation of visual information in the visual cortex, and suggest awake animals have greater capacities to respond to fast changing and/or refined visual stimuli.

Higher visual areas encode complementary representation of visual motion speed

The complete mapping of the spatiotemporal frequency space allowed us to determine individual neurons' tuning for visual motion speed. The speed is given as the ratio of temporal and spatial frequencies. A speed-tuned neuron has similar tuning curves for speed across spatial frequencies, and thus the temporal frequency tuning varies as a function of the spatial frequency tuning. By contrast, a non-speed-tuned cell has separable, independent tuning for the spatial and temporal frequency (Figure 6A – figure supplement 7A). The speed tuning index ξ is the correlation between spatial and temporal frequency, extracted from the Gaussian fits. If $\xi >= 0.5$, neurons are speed tuned; otherwise, untuned. The speed tuning analysis was focused on the responses to isotropic noise stimuli, which contained local motion components rather than

bioRxiv preprint doi: https://doi.org/10.1101/441014; this version posted October 12, 2018. The copyright holder for this preprint (which was not certified by peer review) is the author/funder. All rights reserved. No reuse allowed without permission.

global, coherent motion (such as drifting gratings). The responses to anisotropic noise stimuli were not used given the potential confound induced by the embedded rotatory motion.

The speed tuning index ξ of V1 population was centered around 0, indicating most V1 cells were not tuned for speed (Figure 6B, C). Neurons in higher visual areas were significantly more tuned than V1 neurons (Figure 6B, C; KS tests with Bon, $p<0.01$). Among higher visual areas, AM contained the largest fraction of speed-tuned cells, followed by RL and AL. In comparison, LM, PM and LI contained relatively smaller fractions of speed-tuned cell. Moreover, speed-tuned neurons encoded distinct ranges of speed across areas (Figure 6B, D). V1 and LM were broadly tuned for the intermediate range of speed (peak at 12.5 and 25 deg/s respectively). AL and AM primarily responded to fast-moving stimuli (peak at 100 deg/s); RL neurons selectively responded to extremely fast stimuli (peak at 400 deg/s). By contrast, PM and LI mainly responded to slow motion (peak at 6.25 deg/s). These results suggest mouse visual cortical areas encode distinct ranges of visual motion speed: V1 is largely untuned for speed; LM is broadly tuned; anterior areas and lateral areas selectively encode fast and slow motion respectively.

Increased speed discriminability in higher visual areas

As higher visual areas show distinct selectivities for spatiotemporal features, an interesting question arises: do these areas computationally benefit from such a functional specialization? To investigate the difference of spatiotemporal information processing between areas, we compared how well could information about the stimulus category (spatiotemporal frequencies) could be decoded from the neural population activities. The decoding accuracy increased as a function of population size, showing distinct frequency-specific performances across areas (Figure supplement 8A, B). In V1, decoding accuracies for all frequencies increased rapidly as the population size increased (Figure supplement 8B), reaching 90% average accuracy with ~50 cells (Figure supplement 8C). This high decoding capacity might attribute to the heterogeneous nature of V1 population. With similarly high heterogeneity, LM population also showed great decoding capacity, especially for intermediate spatial frequencies (Figure supplement 8C). By contrast, highly specialized areas showed decreased decoding performance. In these areas, decoding accuracies rose slowly with increasing population sizes; some frequencies could not be successfully discriminated with even very large populations (e.g. RL, accuracy <80% with 1000 neurons; figure supplement 8B). RL showed deteriorated performance across frequencies, with a slight recovery at the intermediate frequencies. AM was better at intermediate frequencies and bad at high spatial frequencies. AL populations, showing

bioRxiv preprint doi: https://doi.org/10.1101/441014; this version posted October 12, 2018. The copyright holder for this preprint (which was not certified by peer review) is the author/funder. All rights reserved. No reuse allowed without permission.

relatively high diversity (Figure 2F), presented elevated performances, especially intermediate spatial frequencies. PM and LI were better at discriminating high spatial frequencies. LI outperformed PM in the decoding performance for intermediate temporal frequencies. The decreased decoding performance for non-preferred frequencies might be just a consequence of absence of responses: no response, no information. Whereas the decrease for preferred frequencies might be due to the absence of diversity, as the stimulus information is low if all neurons respond to it. These results suggested V1 and LM encode holistic information about visual stimuli, whereas distinct spatiotemporal information is distributed across higher visual cortical areas.

Higher visual areas showed higher fractions of speed-tuned neurons than V1, are they better at encoding for speed? We measured decoding performances between stimulus pairs corresponding to distinct local motion speeds (e.g., stimulus S_1T_2 has half spatial frequency and twice temporal frequency as stimulus S_2T_1, thus S_1T_2 is four times faster than S_2T_1; Figure 7B, speed pairs are orthogonal to the iso-speed lines). V1 showed relative homogeneous decoding capacities across speed pairs, showing a slight increase at lower spatial frequencies. LM showed greater decoding capacities for slow to intermediated speed (6.25 – 200 deg/s). AL population clearly separated slow stimuli (12.5-25 deg/s) from intermediate ones (50-100 deg/s). AM and RL were specialized for speed discrimination at intermediate frequencies, albeit RL exhibited a global decrease in decoding performance. LI showed elevated discrimination capacity for the lower range of speed (3.1-100 deg/s). PM showed a similar tendency for better discrimination for slow stimuli, albeit less pronounced as LI. Moreover, the frequency-specific enhancement of speed decoding performances in higher visual areas did not merely reflect individual areas' frequency preferences, since the speed decoding remarkably outperformed the decoding for iso-speed stimulus pairs in the same frequency space (Figure 7B; speed pairs: S_1T_2 vs S_2T_1; compare to Figure 8E; iso-speed pairs: S_1T_1 vs S_2T_2). Altogether, these results demonstrated greater speed discrimination capacities in higher visual areas, with the loss of spatiotemporal discriminability. This finding suggests information lost due to functional specialization is a trade-off for better encoding capacities of novel features, which might arise from integrating non-correlated features by pooling large populations of neurons with specific tuning properties.

Discussion

Mouse higher visual areas are suggested engaged in a wide range of behaviorally relevant visual computations (Harvey et al., 2012; Olcese et al., 2013; Burgess et al., 2016; Morcos and

bioRxiv preprint doi: https://doi.org/10.1101/441014; this version posted October 12, 2018. The copyright holder for this preprint (which was not certified by peer review) is the author/funder. All rights reserved. No reuse allowed without permission.

Harvey, 2017). However, the neural basis of these computations remains poorly understood, largely due to the lack of knowledge of the functional properties of neurons in higher visual areas. Using rich spectral noise stimuli and two-photon calcium imaging, we provide a detailed characterization of the stimulus preference of layer 2/3 neurons in V1 and 6 higher visual areas in awake mice. We found cortical areas showed distinct preference for stimulus anisotropy; area LI showed the most pronounced preference for non-oriented stimuli amongst areas. Moreover, higher visual areas, contrasting V1, contained a substantial fraction of neurons sensitive to the visual motion speed. Area LM, encompassing diverse spatiotemporally tuned neurons, respond to a broad range of speed. Anterior areas (AL, RL and AM) preferentially responded to low spatial, high temporal frequencies, thus fast motion; whereas lateral areas (PM and LI) preferred high spatial, low temporal frequencies, thus slow motion. Population coding analysis further revealed greater speed discriminability in higher visual areas. These findings provide novel insights of a highly specialized network of cortical areas that might underpin distinct visual computations, such as motion and shape processing.

Comparison of spatiotemporal selectivity with previous studies

The preferred spatiotemporal frequencies observed in the current study are remarkably higher (up to 2-fold) than in earlier study on anesthetized mice (Marshel et al., 2011), but comparable to the report on awake mice (Andermann et al., 2011). These results hint to the impact of anesthesia on neuronal responses. The lower ranges of preferred temporal frequencies observed in anesthetized mice (Van Den Bergh et al., 2010; Marshel et al., 2011; Roth et al., 2012; Tohmi et al., 2014) might result from suppressed thalamocortical synaptic transmission (Reinhold et al., 2015). The difference in the spatial frequency tuning is, however, unlikely caused by different anesthetic levels (Zhuang et al., 2014; Durand et al., 2016). One explanation could be differential neuronal populations sampled in these two studies. In Marshel's study (Marshel et al., 2011), excitatory and inhibitory neurons were ubiquitously labeled with the synthetic calcium indicator (Oregon Green Bapta-1 AM); whereas in this study we sampled from a subset of excitatory neurons in Thy1-GCaMP6s transgenic mice (Dana et al., 2014). As V1 interneurons prefer lower spatial frequencies than layer2/3 excitatory neurons (Niell and Stryker, 2008), the population preference would shift towards lower frequencies with the inclusion of interneurons. Nevertheless, it is unclear whether such a difference between excitatory and inhibitory neurons also exist in higher visual areas, and consequently lead to the lower preferred spatial frequencies as a population. Further comparisons of neuronal response properties in wakefulness and anesthesia (Greenberg et al., 2008; Haider et al., 2013; Durand

bioRxiv preprint doi: https://doi.org/10.1101/441014; this version posted October 12, 2018. The copyright holder for this preprint (which was not certified by peer review) is the author/funder. All rights reserved. No reuse allowed without permission.

et al., 2016; Adesnik, 2017) will shed light to the influence of different brain states on the neural representation and transformation among visual cortical areas. Nevertheless, studying neuronal physiology in the awake brain will be of great value for understanding neural computations for perception and behavior.

Selectivity for stimulus anisotropy

We found cortical neurons are highly selective for stimulus anisotropy (Figure 3). As increasing stimulus anisotropy increases the length of oriented bars, this selectivity might reflect a form of length tuning. Many neurons prefer oriented stimuli, with increased responses to longer lengths, resembling a phenomenon known as 'length summation' (Schumer and Movshon, 1984). Meanwhile, many neurons prefer short stimuli, reminiscent of 'end-stopping' cells, who preferentially respond to stimuli of limited lengths (Hubel and Wiesel, 1965; Gilbert, 1977). This length tuning property may be attributed to 'surround suppression', where one receptive field is inhibited by the stimulation at the surround. Diverse length tuning curves may emerge from differential ratios of the excitation on classical receptive fields and the inhibitory effect of the receptive field surround (Adesnik et al., 2012; Vaiceliunaite et al., 2013; Adesnik, 2017).

We found diverse length tuning in all test areas. V1 and LM presented relatively strong biases for non-oriented stimuli, suggesting strong surround suppression that was also found in the primate (Hubel and Livingstone, 1987; Shushruth et al., 2009; El-Shamayleh et al., 2013), cat (DeAngelis et al., 1994) and mouse (Van Den Bergh et al., 2010; Adesnik et al., 2012; Nienborg et al., 2013; Vaiceliunaite et al., 2013; Adesnik, 2017). Surround suppression was also reported in the primate middle temporal visual area (MT/V5) (Born and Bradley, 2005) and suggested to be used to solve the aperture problem (Tsui et al., 2010). Mouse RL was proposed to be the mouse analogue of MT (Juavinett and Callaway, 2015); hence the surround suppression in RL and other dorsal areas (AL, AM and PM) might facilitate unambiguous encoding of motion directions. In the primate, 'end-stopping' behavior increases along the ventral processing stream and is suggested to benefit the coding for curvatures (Ponce et al., 2017). Area LI, showing a pronounced preference for non-oriented stimuli, shares an interesting similarity to the primate ventral areas, suggesting its potential role in the processing of visual shapes.

Functional organization of mouse higher visual areas

Our data demonstrated a complementary representation of visual motion speed in the mouse higher visual areas (Figure 6). Anterior areas (AL, RL and AM) contain abundant speed-tuned cells and encode fast local motion speed (Tohmi et al., 2009, 2014; this study). As anterior areas mainly represent the lower visual field (Zhuang et al., 2017), high-speed tuning properties

bioRxiv preprint doi: https://doi.org/10.1101/441014; this version posted October 12, 2018. The copyright holder for this preprint (which was not certified by peer review) is the author/funder. All rights reserved. No reuse allowed without permission.

of these areas might benefit the encoding for fast optic flows near the ground during animal's navigation. Indeed, area RL, who covers the lower nasal field, where has the fastest optic flows, showed the highest preferred speed. In consistency, anterior area A was reported to preferentially respond to high temporal and low spatial frequencies (Murakami et al., 2017), suggesting the preference for fast speed. In contrast, area PM mainly represents visual peripheries, where objects are usually distant and optic flows are slow. Ethologically, PM neurons show the preference for slow speeds (this study; Andermann et al., 2011; Roth et al., 2012). Interestingly, PM neurons were reported to show strong speed-tuned responses to drifting gratings (Andermann et al., 2011), but showed less prevalence in this study. One explanation is speed-tuned cells in PM are selective for global, coherent motion than local, non-coherent motion (e.g. isotropic noise stimuli). In fact, using noise stimuli embedded in a global directional motion flow, we found PM neurons responded more robustly to coherent motion (data not shown), suggesting the specialization of area PM for encoding slow optic flows in the visual periphery during navigation. PM might provide information about optic flows via the strong direct inputs to retrosplenial cortex (Wang et al., 2012), which preferentially responses to slow motion (Murakami et al., 2015) and is involved in the spatial navigation (Mao et al., 2017). Besides PM, anterior and medial areas mainly target parietal, motor and limbic cortices (Wang et al., 2012), coinciding with the representation of visuospatial functions in the dorsal stream in rats (Kolb and Walkey, 1987). Altogether, the distinct preference for visual motion speed in dorsal areas (AL, RL, AM and PM) suggest an ethological coding of optic flows during navigation, reminiscent of the dorsal streams in the primate visual system (Van Essen and Maunsell, 1983).

Lateral area LI presents preferences for spatial details and non-oriented stimuli (Figure 3-5). These properties are suitable for encoding spatial details and curvatures, and are critical for object recognition in the primate ventral stream (Ponce et al., 2017; Lu et al., 2018). In addition, anatomical studies suggested area LI is a node in the ventral stream: most of the projections terminate in temporal and parahippocampal regions (Wang et al., 2012). These pieces of evidence suggest area LI belongs to the ventral stream for shape processing (analogous area in the rat: Vermaercke et al., 2014; Tafazoli et al., 2017; in the primate: Van Essen and Maunsell, 1983). Rat lateral areas, including LI, presenting increased transformation-tolerant representation of visual objects(Vermaercke et al., 2014; Tafazoli et al., 2017). It poses interests for future studies to determine if a similar representation exists in the mouse lateral areas, and how does it make use of the specialized tuning properties of simple features for more complex representations, such as visual objects.

bioRxiv preprint doi: https://doi.org/10.1101/441014; this version posted October 12, 2018. The copyright holder for this preprint (which was not certified by peer review) is the author/funder. All rights reserved. No reuse allowed without permission.

Area LM was proposed to be the gateway for the ventral stream (AL as the gateway for the dorsal stream), given its relatively denser projections to the ventral areas (Wang et al., 2011, 2012) and population responses relatively similar to the ventral areas (wide field imaging in Murakami et al., 2017; Smith et al., 2017). Our data showed, however, LM contains highly diverse neurons that present dorsal and ventral properties, resembling the primate V2 (Van Den Bergh et al., 2010). In addition, LM neurons send strong projections to all other higher visual areas (Wang et al., 2011, 2012), conveying target-specific information (Glickfeld et al., 2013). The functional properties of LM neurons suggest its role as the divided gateway of dorsal and ventral streams.

Conclusion

The current study provides a comprehensive characterization of stimulus presences of layer 2/3 neurons in V1 and higher visual areas in awake mice. The results reveal the segregation of spatiotemporal features in the visual cortex that might underpinning the processing of visual motion and shape. Facing the accumulating evidence of higher order computations in the mouse higher visual cortex (Olcese et al., 2013; Burgess et al., 2016; Morcos and Harvey, 2017), it is essential to understand how area-specific representations of visual features arise along the visual hierarchy, and how basic features of visual and other sensory information are integrated in the higher order cortex for complex computations. The results and implication of this study, provide a necessary basis for future studies investigating circuitry mechanisms for visual perception and behaviors.

Materials and Methods

Animals and Surgery

All experiments were conducted with the approval of the Animal Ethics Committee of KU Leuven. Standard craniotomy surgeries were performed to gain optical access to the visual cortex through a set of cover glasses (Goldey et al., 2014). Thy1- GCaMP6s-WPRE (Dana et al. 2014) mice (n = 10, 5 male and 5 female) between 2 and 3-month-old were anesthetized with isoflurane (2.5%–3% induction, 1%–1.25% surgery). A custom-made titanium frame was mounted to the skull, and a craniotomy over the visual cortex was made for calcium imaging. The cranial window was covered by a 5mm cover glass. Buprenex and Cefazolin were

bioRxiv preprint doi: https://doi.org/10.1101/441014; this version posted October 12, 2018. The copyright holder for this preprint (which was not certified by peer review) is the author/funder. All rights reserved. No reuse allowed without permission.

administered postoperatively (2 mg/kg and 5 mg/kg respectively) when the animal recovered from anesthesia after surgery.

Widefield Calcium Imaging

Widefield fluorescent images were acquired through a 2x objective (NA = 0.055, Edmund Optics). Illumination was from a blue LED (479nm, ThorLabs), the green fluorescence was collected with an EMCCD camera (EM-C^2, QImaging) via a bandpass filter (510/84 nm filter, Semrock). The image acquisition was controlled with a customize software.

Two-photon Calcium Imaging

A customized two-photon microscopy (Neurolabware) was used. GCaMP6s were excited at 920nm wavelength with a Ti:Sapphire excitation laser (MaiTai DeepSee, Spectra-Physics). The green fluorescence of GCaMP6s was collected with a photomultiplier tube (PMT, Hamamatsu) through a bandpass filter (510/84 nm, Semrock). Images (720x512 pixel per frame) were collect at 31 Hz with a 16x objective (Nikon). Volume imaging was performed using a focus tunable lens (EL-10-30-TC, Optotune; staircase mode). We simultaneously recorded neuronal activities in large volumes (0.8 x 0.8 x 0.15 mm^3) of layer 2/3 of the targeted visual cortical areas. During imaging, mice were head-clamped on a platform while consciously viewing the visual stimuli on the display. Eye movements were monitors using a camera and infrared illumination (720–900 nm bandpass filters, Edmund).

Visual Stimulation

Visual stimuli were displayed on a gamma-corrected LCD display (22'', Samsung 2233RZ). The screen was oriented parallel to the eye and placed 18 cm from the animal (covering 80 degree in elevation by 105 degree in azimuth). Spherical correction was applied to the stimuli to define eccentricity in spherical coordinates.

Spectral noise stimuli (Figure supplement 2) were created by applying a set of parametrized filters on random pink-noise movies. Bandpass filters (bandwidth: 1 octave) with different center spatial frequencies (0.02, 0.04, 0.08, 0.16 and 0.32 cpd) and temporal frequencies (0.5, 1, 2, 4, 8, 16 Hz) gave 30 combinations of spatiotemporal noises. Cutoff frequencies were set at 0.5 octave lower or higher than the center frequencies. A Von Mise filter was used to control the orientation bandwidth (no filter, 40, 10, 5 degree) in the spatial frequency domain, and thus the stimulus anisotropy in the space domain. Isotropic (ISO) and anisotropic (ANISO) noise stimuli were used for the spatiotemporal frequency assay. ISO stimuli contained non-oriented patterns, resembling clouds of dots with alternating contrast. In contrast, ANISO stimuli, with a narrow

bioRxiv preprint doi: https://doi.org/10.1101/441014; this version posted October 12, 2018. The copyright holder for this preprint (which was not certified by peer review) is the author/funder. All rights reserved. No reuse allowed without permission.

orientation bandwidth (5 degree), presented oriented patterns that resembles sinusoidal gratings. Each stimulus set comprises an array of 30 combinations of spatial frequencies (0.02, 0.04, 0.08, 0.16, 0.32 cycle per degree) and temporal frequencies (0.5, 1, 2, 4,8,16 Hz), spanning a broad frequency spectrum. In addition, ANISO stimuli smoothly rotated 180 degree to sweep the orientation space within each stimulus epoch. For the stimulus anisotropy assay, the stimulus set comprised pairs of four degrees of orientation bandwidth (infinite, 40, 10, 5 degree) and four center spatial frequencies (0.04, 0.08, 0.16, 0.32 cpd), with a fixed center temporal frequency (2Hz). A global rotation was also applied to sweep the orientation space. Each stimulus condition was presented for 4 second, intertwined with 4-second equiluminent gray screen. In each of the four pseudorandomized trials, a different seed was used to generated unique random noise, resulting different phases yet constant frequency spectra across trials.

For retinotopic mapping, we presented two sets of stimuli. Circling patch stimuli had a small patch (20-degree in diameter) circling along an elliptic trajectory (azimuth: -40 to 40 deg; elevation: -30 to 30 deg) on the display. Traveling bar stimuli comprised a narrow bar (13 deg wide) sweeping across the screen in 4 cardinal direction. An isotropic noise background (0.08 cpd, 2Hz) was embedded in the patch or bar. Each stimulus condition lasted for 10 seconds and repeated for 20 times.

Data Analysis

All subsequent data analysis was performed in MATLAB (The Mathworks, Natick, MA).

Retinotopy analysis

The phase maps were measured form the fluorescent responses to the phase/position of the circling patch stimuli (Figure supplement 1). Each area has a representation of the elliptic trajectory of the patch, resulting pinwheel-like retinotopic maps. Sign maps were obtained with the methods described in the previous study (Garrett et al., 2014). Azimuth and elevation position maps were measured as the temporal phase of the peak florescent responses to a traveling bar for each pixel. They were used to generate a visual field sign map, where each patch represented one cortical area.

Selection for visual cells

For the cellular imaging, raw images were reconstructed and corrected for brain motion artefacts using custom MATLAB routines (Bonin et al. 2011). Regions of interest (ROI) were

bioRxiv preprint doi: https://doi.org/10.1101/441014; this version posted October 12, 2018. The copyright holder for this preprint (which was not certified by peer review) is the author/funder. All rights reserved. No reuse allowed without permission.

selected with custom semi-automated segmentation algorithms. Cellular fluorescence time courses were generated by averaging all pixels in a cell mask, followed by subtracting the neuropil signals in the surround shell. Responses were defined as the averaged dF/F during the stimulus epoch, where dF is the change in the fluorescent signal and F is the baseline fluorescence.

Neurons were considered responsive to a given stimuli if responding to at least one stimulus condition (median response surpass 3x standard deviation of the baseline fluctuation for over 1 second). Response reliability was measured in two ways, (1) coefficient variation of the responses to the peak frequencies across trials, and (2) the average trial-to-trial correlation of the fluorescent time courses. Neurons above threshold (trial-to-trial correlation ≥ 0.4) were deemed reliable.

Clustering

The population response matrices for each area were generated with random selection of 2000 neurons, each of which was represented as a vector of responses to ISO and ANISO stimuli (normalized to range from 0 to 1). The response matrix of the populations across all areas were used in a spectral clustering algorithm (Matlab Central). To determine whether there are discrete functional types, we plotted the overall variances (within-cluster sum-of-square) as a function of number of clusters. We didn't observe abrupt decrease of variance with increased cluster size (Figure supplement 4A), suggesting there are no discrete functional response types but rather a continuum. Anyways we used the clustering approach to study the population response profiles across areas. We decided on the selection of 12 clusters for low heterogeneity within clusters without excessive splitting (Figure supplement 4B).

Tuning curves

For the spatial and temporal frequency analysis, responses were fit to two-dimensional elliptical Gaussian models (Priebe et al. 2003; Andermann et al. 2011):

$$R(sf, tf) = A \exp\left(\frac{-(\log_2 sf - \log_2 sf_0)^2}{2(\sigma_{sf})^2}\right) \exp\left(\frac{-(\log_2 tf - \log_2 tf_p(sf))^2}{2(\sigma_{tf})^2}\right),$$

where $\log_2 tf_p(sf) = \xi(\log_2 sf - \log_2 sf_0) + \log_2 tf_0$, and A is the peak response amplitude, sf_0 and tf_0 are the preferred spatial and temporal frequencies, and σ_{sf} and σ_{tf} are the spatial and temporal frequency tuning widths. The dependence of temporal frequency preference on spatial frequency is captured by a power-law exponent x. Estimates of cutoff values for spatial and

bioRxiv preprint doi: https://doi.org/10.1101/441014; this version posted October 12, 2018. The copyright holder for this preprint (which was not certified by peer review) is the author/funder. All rights reserved. No reuse allowed without permission.

temporal frequency were obtained from the half maxima of cross- sections at $R(sf, tf_0)$ and $R(sf_0, tf)$, respectively. Neurons responding to the lowest tested frequencies with over 50% peak responses were categorized as lowpass, and thus the low cutoff values were set to the lowest frequencies. In the same manner, the high cutoff values of highpass cells were set to the highest tested frequencies. Half-width bandwidths were estimated from bandpass cells.

Tuning curves for stimulus anisotropy were measured as the average responses to different degrees of stimulus anisotropy at the preferred spatial frequencies. The stimulus anisotropy index (SAI) was the difference/sum ratio of response amplitudes to the most anisotropic stimuli and the isotropic stimuli.

$$SAI = \frac{R(aniso) - R(iso)}{R(aniso) + R(iso)}$$

Population coding analysis

We used linear classifiers to decode stimulus categories from neuronal population activities (Vermaercke et al., 2014). SVM (support vector machine) was trained and tested in pair-wise classification for each possible pair (30 stimulus conditions in 435 unique pairs). Population used for frequency classification were composed of neurons responding to isotropic noise stimuli. Data were split into training and testing groups (half-half) and performance was measured as the proportion of correct classification decisions to the testing groups (standard cross validation). To test the scaling of decoding performance as a function of population size, we measured the decoding performances with subsamples of different numbers of neurons (logistic increase, 1 to 1000; without replacement) across areas. For each iteration, we resampled neuronal populations with specific population size. We averaged over 100 iterations to obtain confidence intervals for the performance. To compare the decoding capacity between stimulus pairs and across areas, we measured the number of neurons required for classification accuracy over 90% by interpolate the growth curves of performances as a function of population size.

Acknowledgements

We thank Steffen Kandler for surgery training and Joao Couto for help with imaging setup and data analysis. XH was supported by a PhD scholarship from the Chinese Scholarship Council. BV was supported by postdoctoral scholarship from FWO (12E4314N). VB acknowledges

bioRxiv preprint doi: https://doi.org/10.1101/441014; this version posted October 12, 2018. The copyright holder for this preprint (which was not certified by peer review) is the author/funder. All rights reserved. No reuse allowed without permission.

support from FWO (Grant G0D0516N), KU Leuven Research Council (Grant C14/16/048) and NERF Institutional Funding. NERF is funded by Imec, VIB and KU Leuven.

Author Contributions

XH and VB designed the research; XH acquired the data; XH, BV performed the data analysis and wrote the paper with input from VB. The authors declare no competing interests.

References

Aasebø IEJ, Lepperød ME, Stavrinou M, Nøkkevangen S, Einevoll G, Hafting T, Fyhn M (2017) Temporal Processing in the Visual Cortex of the Awake and Anesthetized Rat. Eneuro 4:ENEURO.0059-17.2017.

Adesnik H (2017) Synaptic Mechanisms of Feature Coding in the Visual Cortex of Awake Mice. Neuron 95:1147–1159.e4.

Adesnik H, Bruns W, Taniguchi H, Huang ZJ, Scanziani M (2012) A neural circuit for spatial summation in visual cortex. Nature 490:226–231.

Andermann ML, Kerlin AM, Roumis DK, Glickfeld LL, Reid RC (2011) Functional specialization of mouse higher visual cortical areas. Neuron 72:1025–1039.

Born RT, Bradley DC (2005) STRUCTURE AND FUNCTION OF VISUAL AREA MT. Annu Rev Neurosci 28:157–189.

Brigman JL, Bussey TJ, Saksida LM, Rothblat LA (2005) Discrimination of multidimensional visual stimuli by mice: Intra- and extradimensional shifts. Behav Neurosci 119:839–842.

Burgess CR, Ramesh RN, Sugden AU, Levandowski KM, Minnig MA, Fenselau H, Lowell BB, Andermann ML (2016) Hunger-Dependent Enhancement of Food Cue Responses in Mouse Postrhinal Cortex and Lateral Amygdala. Neuron 91:1154–1169.

Chen G, King JA, Burgess N, O'Keefe J (2013) How vision and movement combine in the hippocampal place code. Proc Natl Acad Sci 110:378–383.

Dana H, Chen T-W, Hu A, Shields BC, Guo C, Looger LL, Kim DS, Svoboda K (2014) Thy1-GCaMP6 Transgenic Mice for Neuronal Population Imaging In Vivo. PLoS One 9:e108697.

DeAngelis GC, Freeman RD, Ohzawa I (1994) Length and width tuning of neurons in the cat's primary visual cortex. J Neurophysiol 71:347–374.

bioRxiv preprint doi: https://doi.org/10.1101/441014; this version posted October 12, 2018. The copyright holder for this preprint (which was not certified by peer review) is the author/funder. All rights reserved. No reuse allowed without permission.

Durand S, Iyer R, Mizuseki K, de Vries S, Mihalas S, Reid RC (2016) A Comparison of Visual Response Properties in the Lateral Geniculate Nucleus and Primary Visual Cortex of Awake and Anesthetized Mice. J Neurosci 36:12144–12156.

El-Shamayleh Y, Kumbhani RD, Dhruv NT, Movshon JA (2013) Visual response properties of V1 neurons projecting to V2 in macaque. J Neurosci 33:16594–16605.

Garrett ME, Nauhaus I, Marshel JH, Callaway EM (2014) Topography and Areal Organization of Mouse Visual Cortex. J Neurosci 34:12587–12600.

Gilbert CD (1977) Laminar differences in receptive field properties of cells in cat primary visual cortex. J Physiol 268:391–421.

Glickfeld LL, Andermann ML, Bonin V, Reid RC (2013) Cortico-cortical projections in mouse visual cortex are functionally target specific. Nat Neurosci 16:219–226.

Goldey GJ, Roumis DK, Glickfeld LL, Kerlin AM, Reid RC, Bonin V, Schafer DP, Andermann ML (2014) Removable cranial windows for long-term imaging in awake mice. Nat Protoc 9:2515–2538.

Greenberg DS, Houweling AR, Kerr JND (2008) Population imaging of ongoing neuronal activity in the visual cortex of awake rats. Nat Neurosci 11:749–751.

Haider B, Häusser M, Carandini M (2013) Inhibition dominates sensory responses in the awake cortex. Nature 493:97–102.

Han Y, Kebschull JM, Campbell RAA, Cowan D, Imhof F, Zador AM, Mrsic-Flogel TD (2018) The logic of single-cell projections from visual cortex. Nature 556:51–56.

Harvey CD, Coen P, Tank DW (2012) Choice-specific sequences in parietal cortex during a virtual-navigation decision task. Nature 484:62–68.

Harvey CD, Collman F, Dombeck D a, Tank DW (2009) Intracellular dynamics of hippocampal place cells during virtual navigation. Nature 461:941–946.

Hoy JL, Yavorska I, Wehr M, Niell CM (2016) Vision Drives Accurate Approach Behavior during Prey Capture in Laboratory Mice. Curr Biol:1–7.

Hubel D, Wiesel T (1965) Receptive field and functional architechture in two nonstriate visual areas (18 and 19) of the cat. J Neurophysiol 28:229–289.

Hubel DH, Livingstone MS (1987) Segregation of form, color, and stereopsis in primate area 18.

bioRxiv preprint doi: https://doi.org/10.1101/441014; this version posted October 12, 2018. The copyright holder for this preprint (which was not certified by peer review) is the author/funder. All rights reserved. No reuse allowed without permission.

J Neurosci 7:3378–3415.

Juavinett AL, Callaway EM (2015) Pattern and Component Motion Responses in Mouse Visual Cortical Areas. Curr Biol 25:1–6.

Ko H, Cossell L, Baragli C, Antolik J, Clopath C, Hofer SB, Mrsic-Flogel TD (2013) The emergence of functional microcircuits in visual cortex. Nature 496:96–100.

Ko H, Hofer SB, Pichler B, Buchanan K a, Sjöström PJ, Mrsic-Flogel TD (2011) Functional specificity of local synaptic connections in neocortical networks. Nature 473:87–91.

Kolb B, Walkey J (1987) Behavioural and anatomical studies of the posterior parietal cortex in the rat. Behav Brain Res 23:127–145.

Liang L, Fratzl A, Goldey G, Ramesh RN, Sugden AU, Morgan JL, Chen C, Andermann ML (2018) A Fine-Scale Functional Logic to Convergence from Retina to Thalamus. Cell 173:1343–1355.e24.

Lien AD, Scanziani M (2013) Tuned thalamic excitation is amplified by visual cortical circuits. Nat Neurosci 16:1315–1323.

Lien AD, Scanziani M (2018) Cortical direction selectivity emerges at convergence of thalamic synapses. Nature 558:80–86.

Lu Y, Yin J, Chen Z, Gong H, Liu Y, Qian L, Li X, Liu R, Andolina IM, Wang W (2018) Revealing Detail along the Visual Hierarchy: Neural Clustering Preserves Acuity from V1 to V4. Neuron:417–428.

Mao D, Kandler S, McNaughton BL, Bonin V (2017) Sparse orthogonal population representation of spatial context in the retrosplenial cortex. Nat Commun 8.

Marques T, Summers MT, Fioreze G, Fridman M, Dias RF, Feller MB, Petreanu L (2018) A Role for Mouse Primary Visual Cortex in Motion Perception. Curr Biol 28:1703–1713.e6.

Marshel JH, Garrett ME, Nauhaus I, Callaway EM (2011) Functional specialization of seven mouse visual cortical areas. Neuron 72:1040–1054.

Maruoka H, Nakagawa N, Tsuruno S, Sakai S, Yoneda T, Hosoya T (2017) Lattice system of functionally distinct cell types in the neocortex. Science (80-) 358:610–615.

Morcos AS, Harvey CD (2017) Evidence Accumulation in Cortex. 19:1672–1681.

bioRxiv preprint doi: https://doi.org/10.1101/441014; this version posted October 12, 2018. The copyright holder for this preprint (which was not certified by peer review) is the author/funder. All rights reserved. No reuse allowed without permission.

Murakami T, Matsui T, Ohki K (2017) Functional Segregation and Development of Mouse Higher Visual Areas. J Neurosci:0731-17.

Murakami T, Yoshida T, Matsui T, Ohki K (2015) Wide-field Ca2+ imaging reveals visually evoked activity in the retrosplenial area. Front Mol Neurosci 08:1–12.

Niell CM, Stryker MP (2008) Highly selective receptive fields in mouse visual cortex. J Neurosci 28:7520–7536.

Nienborg H, Hasenstaub A, Nauhaus I, Taniguchi H, Huang ZJ, Callaway EM (2013) Contrast dependence and differential contributions from somatostatin- and parvalbumin-expressing neurons to spatial integration in mouse V1. J Neurosci 33:11145–11154.

Nithianantharajah J, Komiyama NH, McKechanie A, Johnstone M, Blackwood DH, Clair DS, Emes RD, Van De Lagemaat LN, Saksida LM, Bussey TJ, Grant SGN (2013) Synaptic scaffold evolution generated components of vertebrate cognitive complexity. Nat Neurosci 16:16–24.

Olcese U, Iurilli G, Medini P (2013) Cellular and synaptic architecture of multisensory integration in the mouse neocortex. Neuron 79:579–593.

Ponce CR, Hartmann TS, Livingstone MS (2017) End-Stopping Predicts Curvature Tuning along the Ventral Stream. J Neurosci 37:648–659.

Poort J, Khan AG, Pachitariu M, Nemri A, Orsolic I, Krupic J, Bauza M, Sahani M, Keller GB, Mrsic-Flogel TD, Hofer SB (2015) Learning Enhances Sensory and Multiple Non-sensory Representations in Primary Visual Cortex. Neuron 86:1478–1490.

Priebe NJ, Cassanello CR, Lisberger SG (2003) The neural representation of speed in macaque area MT/V5. J Neurosci 23:5650–5661.

Prusky GT, West PW., Douglas RM (2000) Behavioral assessment of visual acuity in mice and rats. Vision Res 40:2201–2209.

Reinhold K, Lien AD, Scanziani M (2015) Distinct recurrent versus afferent dynamics in cortical visual processing. Nat Neurosci:1–15.

Roth MM, Helmchen F, Kampa BM (2012) Distinct functional properties of primary and posteromedial visual area of mouse neocortex. J Neurosci 32:9716–9726.

Schumer RA, Movshon MSL a. JA (1984) Length summation in simple cells of cat striate cortex.

bioRxiv preprint doi: https://doi.org/10.1101/441014; this version posted October 12, 2018. The copyright holder for this preprint (which was not certified by peer review) is the author/funder. All rights reserved. No reuse allowed without permission.

Vis Res 24:565–571.

Shushruth S, Ichida JM, Levitt JB, Angelucci A (2009) Comparison of Spatial Summation Properties of Neurons in Macaque V1 and V2. J Neurophysiol 102:2069–2083.

Smith IT, Townsend LB, Huh R, Zhu H, Smith SL (2017) Stream-dependent development of higher visual cortical areas. Nat Neurosci:1–11.

Stirman JN, Townsend LB, Smith SL (2016) A touchscreen based global motion perception task for mice. Vision Res 127:74–83.

Tafazoli S, Safaai H, De Franceschi G, Rosselli FB, Vanzella W, Riggi M, Buffolo F, Panzeri S, Zoccolan D (2017) Emergence of transformation-tolerant representations of visual objects in rat lateral extrastriate cortex. Elife 6:1–39.

Tohmi M, Meguro R, Tsukano H, Hishida R, Shibuki K (2014) The Extrageniculate Visual Pathway Generates Distinct Response Properties in the Higher Visual Areas of Mice. Curr Biol:1–11.

Tohmi M, Takahashi K, Kubota Y, Hishida R, Shibuki K (2009) Transcranial flavoprotein fluorescence imaging of mouse cortical activity and plasticity. J Neurochem 109:3–9.

Tsui JMG, Hunter JN, Born RT, Pack CC (2010) The Role of V1 Surround Suppression in MT Motion Integration. J Neurophysiol 103:3123–3138.

Vaiceliunaite A, Erisken S, Franzen F, Katzner S, Busse L (2013) Spatial integration in mouse primary visual cortex. J Neurophysiol 110:964–972.

Van Den Bergh G, Zhang B, Arckens L, Chino YM (2010) Receptive-field properties of V1 and V2 neurons in mice and macaque monkeys. J Comp Neurol 518:2051–2070.

Van Essen DC, Maunsell JHR (1983) Hierarchical organization and functional streams in the visual cortex. Trends Neurosci 6:370–375.

Vermaercke B, Gerich FJ, Ytebrouck E, Arckens L, Op de Beeck HP, Van den Bergh G (2014) Functional specialization in rat occipital and temporal visual cortex. J Neurophysiol:jn.00737.2013.

Wang Q, Burkhalter A (2011) Area Map of Mouse Visual Cortex. J Comp Neurol 502:275–290.

Wang Q, Gao E, Burkhalter A (2011) Gateways of ventral and dorsal streams in mouse visual cortex. Sci Signal 31:1905–1918.

bioRxiv preprint doi: https://doi.org/10.1101/441014; this version posted October 12, 2018. The copyright holder for this preprint (which was not certified by peer review) is the author/funder. All rights reserved. No reuse allowed without permission.

Wang Q, Sporns O, Burkhalter A (2012) Network analysis of corticocortical connections reveals ventral and dorsal processing streams in mouse visual cortex. J Neurosci 32:4386–4399.

Wanner A, Zhang C, Roth CN, Yonehara K, Wanner A, Zhang C, Roth CN, Yonehara K (2017) Different Modes of Visual Integration in the Lateral Geniculate Nucleus Revealed by Single-Cell-Initiated Transsynaptic Tracing. :767–776.

Zhuang J, Bereshpolova Y, Stoelzel CR, Huff JM, Hei X, Alonso J-M, Swadlow H a. (2014) Brain State Effects on Layer 4 of the Awake Visual Cortex. J Neurosci 34:3888–3900.

Zhuang J, Ng L, Williams D, Valley M, Li Y, Garrett M, Waters J (2017) An extended retinotopic map of mouse cortex. Elife 6:1–29.

bioRxiv preprint doi: https://doi.org/10.1101/441014; this version posted October 12, 2018. The copyright holder for this preprint (which was not certified by peer review) is the author/funder. All rights reserved. No reuse allowed without permission.

Figures and figure captions

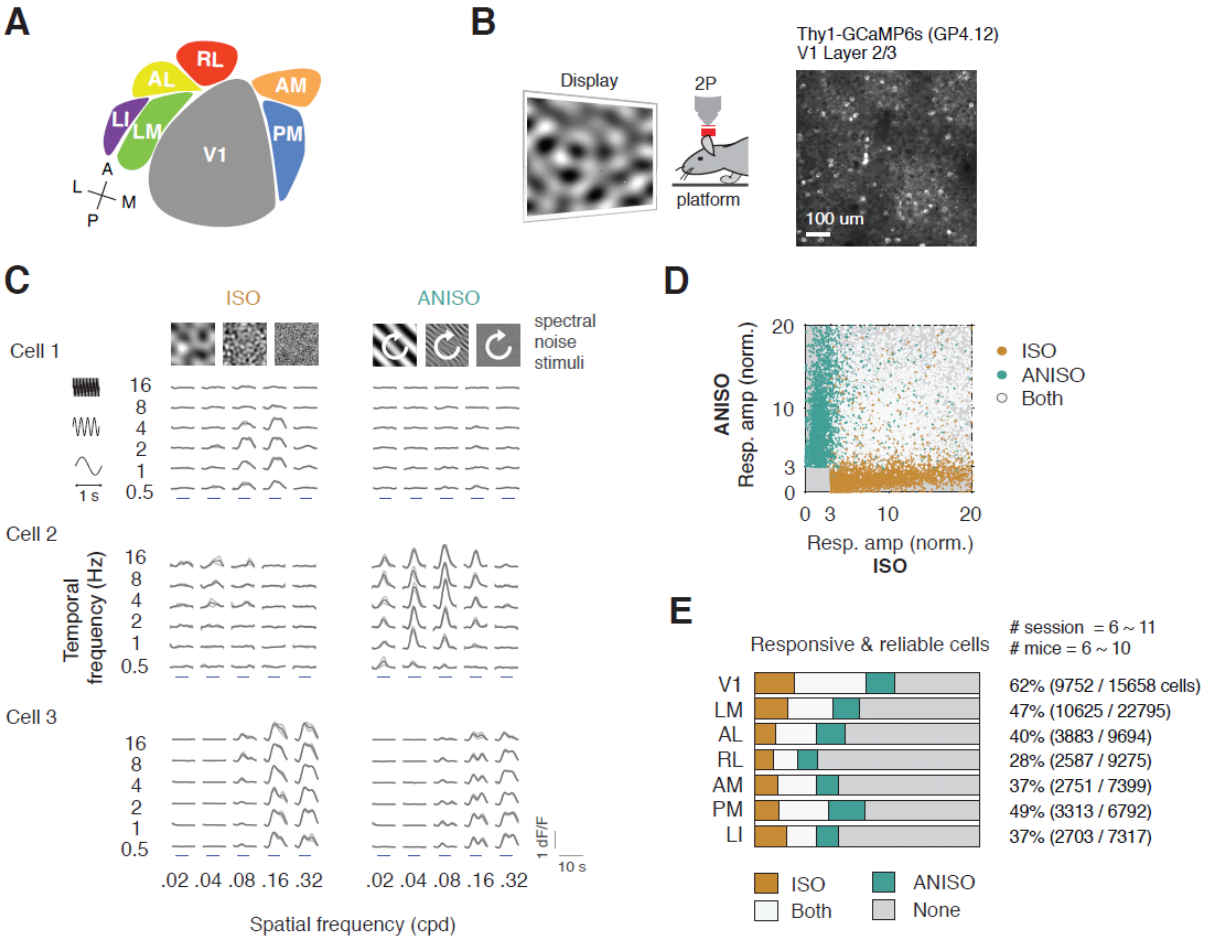

Figure 1. Spectral noise stimuli activate distinct populations in multiple visual cortical areas. (A) Scheme showing V1 and six higher visual areas tested in this study. (B) Experimental setup for two-photon calcium imaging on awake mice. Left panel: Mice were placed on a platform while cellular responses to spectral noise stimuli were recorded using two photon calcium imaging. Right panel: example field of view of the layer2/3 population in V1 of Thy-GCaMP6s (GP4.12) mice. Scale bar: 100um. (C) Example cells showing distinct responses to ISO and ANISO stimuli. ISO stimuli are non-oriented stimuli with isotropic spatial frequencies (left upper row). ANISO stimuli are oriented stimuli with a clockwisely rotatory sweep within each stimulus epoch (right upper row). Both ISO and ANISO stimuli contain the combination of five spatial frequencies (0.02, 0.04, 0.08, 0.16, 0.32 cpd) and six temporal frequencies (0.5, 1, 2, 4, 8, 16 Hz). See figure supplement 2 for detailed description of the spectral noise stimuli. The gray lines show the median values of the responses to different spatiotemporal frequencies across trials. The median absolute deviations across trials are shown as light gray shadow. Cell

bioRxiv preprint doi: https://doi.org/10.1101/441014; this version posted October 12, 2018. The copyright holder for this preprint (which was not certified by peer review) is the author/funder. All rights reserved. No reuse allowed without permission.

1 and 2 selectively respond to ISO and ANISO stimuli respectively, while cell 3 shows similar responses to both stimuli. Blue bars indicate the 4-sec stimulus epochs. dF/F: ratio of fluorescent changes. (D) Scatter plot showing z-scored responses (mean/standard deviation across trials) to ISO and ANISO stimuli of all neurons. Neurons are classed into three groups: responding solely to ISO or ANISO stimuli, or to both. (E) Bar plot showing the fractions of neurons responding to either ISO or ANISO stimuli or both within and across areas. Non-responsive cells were shown in gray. See figure supplement 3 for the selection criteria for responsive and reliable cells.

The following figure supplements is available for figure 1:

Figure supplement 1: Identification of mouse visual cortical areas.

Figure supplement 2: Spectral noise stimuli.

Figure supplement 3: Higher visual area neurons have lower responsiveness and response reliability.

bioRxiv preprint doi: https://doi.org/10.1101/441014; this version posted October 12, 2018. The copyright holder for this preprint (which was not certified by peer review) is the author/funder. All rights reserved. No reuse allowed without permission.

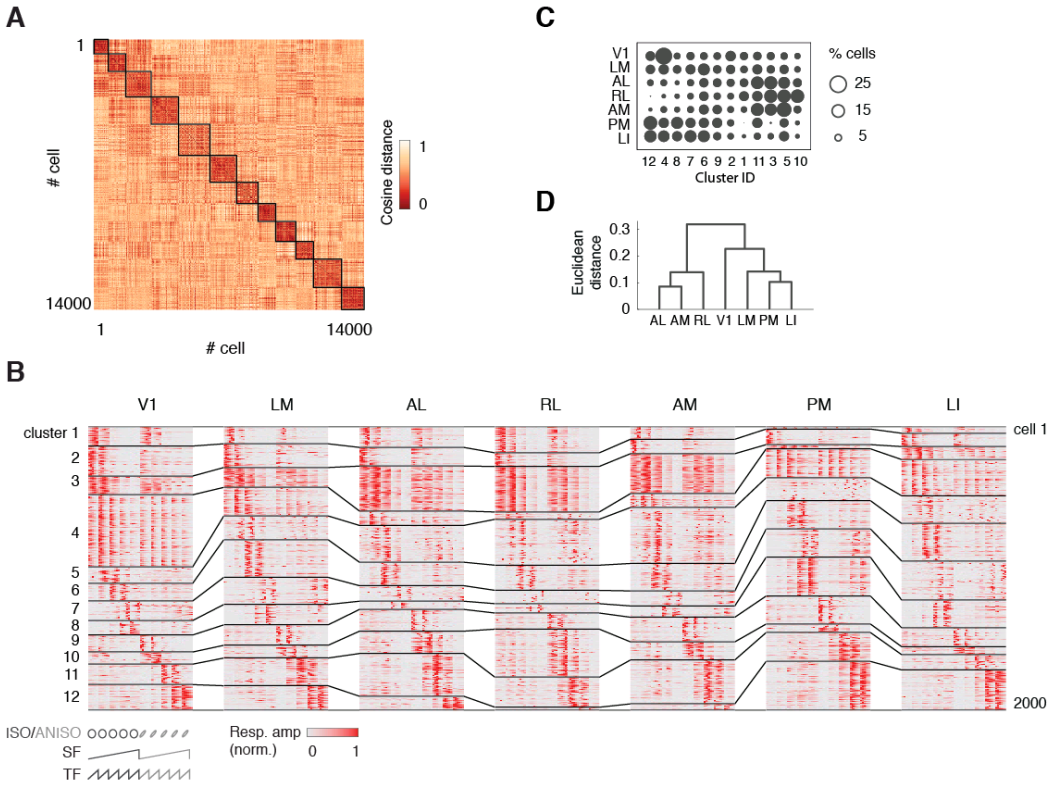

Figure 2: Segregation of population response profiles across cortical areas. (A) Heat map showing the cosine distances between the response profiles of 2000 randomly selected neurons per area (14000 neurons in total). Black boxes delineate the 12 clusters. (B) Matrices showing population response profiles across areas. Each matrix comprises the response profiles of 2000 randomly selected neurons. Each row is the peak-normalized response profile of a single neuron. Cells are clustered into 12 broad functional groups based on the similarity of response profiles using spectral clustering approach (Materials and methods). The black lines delineate neighboring groups and connect the same groups across matrices. The stimulus parameters are annotated below the V1 matrix. (C) Dot plot presenting the proportion of functional groups across areas. The groups are sorted to demonstrate the similarities and differences between areas. (D) Hierarchical tree showing the dissimilarity between areas in the Euclidean distances estimated from the population composition across areas.

The following figure supplements is available for figure 2:

Figure supplement 4: Clustering.

Figure supplement 5: Response properties of functional groups.

bioRxiv preprint doi: https://doi.org/10.1101/441014; this version posted October 12, 2018. The copyright holder for this preprint (which was not certified by peer review) is the author/funder. All rights reserved. No reuse allowed without permission.

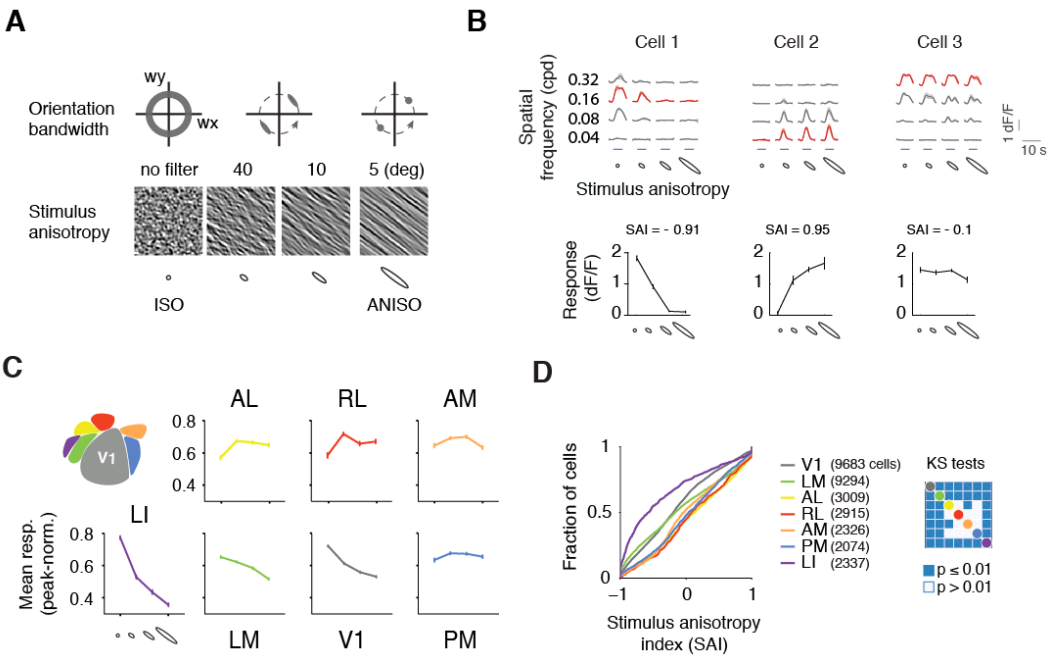

Figure 3: Distinct preferences for the stimulus anisotropy across cortical areas. (A) Example noise stimuli showing increasing stimulus anisotropies corresponding to increasingly narrow orientation bandwidths. Bandpass noises without orientation filters are non-oriented stimuli (ISO stimuli). The narrowest orientation bandwidth (5 degree) corresponds to the ANISO stimuli. (B) Example cells showing distinct responses to combinations of spatial frequencies and stimulus anisotropies (upper panels). These cells correspond to the example cells in Figure 1C, showing matched response preferences for ISO and ANISO stimuli. Tuning curves for stimulus anisotropy were measured at the preferred spatial frequencies (red curves), and are shown in the lower panels. The stimulus anisotropy index (SAI) is the difference/sum ratio of the responses to isotropic and most anisotropic conditions. SAI close to -1 means the preference for isotropy; 1 for anisotropy. (C) Population tuning curves for stimulus anisotropy across areas. Each line is the average of peak-normalized tuning curves within each area. Areas are arranged to present the relative anatomical organization. Top row: anterior areas; bottom row: posterior areas. Left to right: lateral to medial. Inset: scheme of cortical areas. (D) Comparison of the distribution of stimulus anisotropy index across areas. The right panel shows statistical comparisons between areas (KS tests with Bonferroni correction).

bioRxiv preprint doi: https://doi.org/10.1101/441014; this version posted October 12, 2018. The copyright holder for this preprint (which was not certified by peer review) is the author/funder. All rights reserved. No reuse allowed without permission.

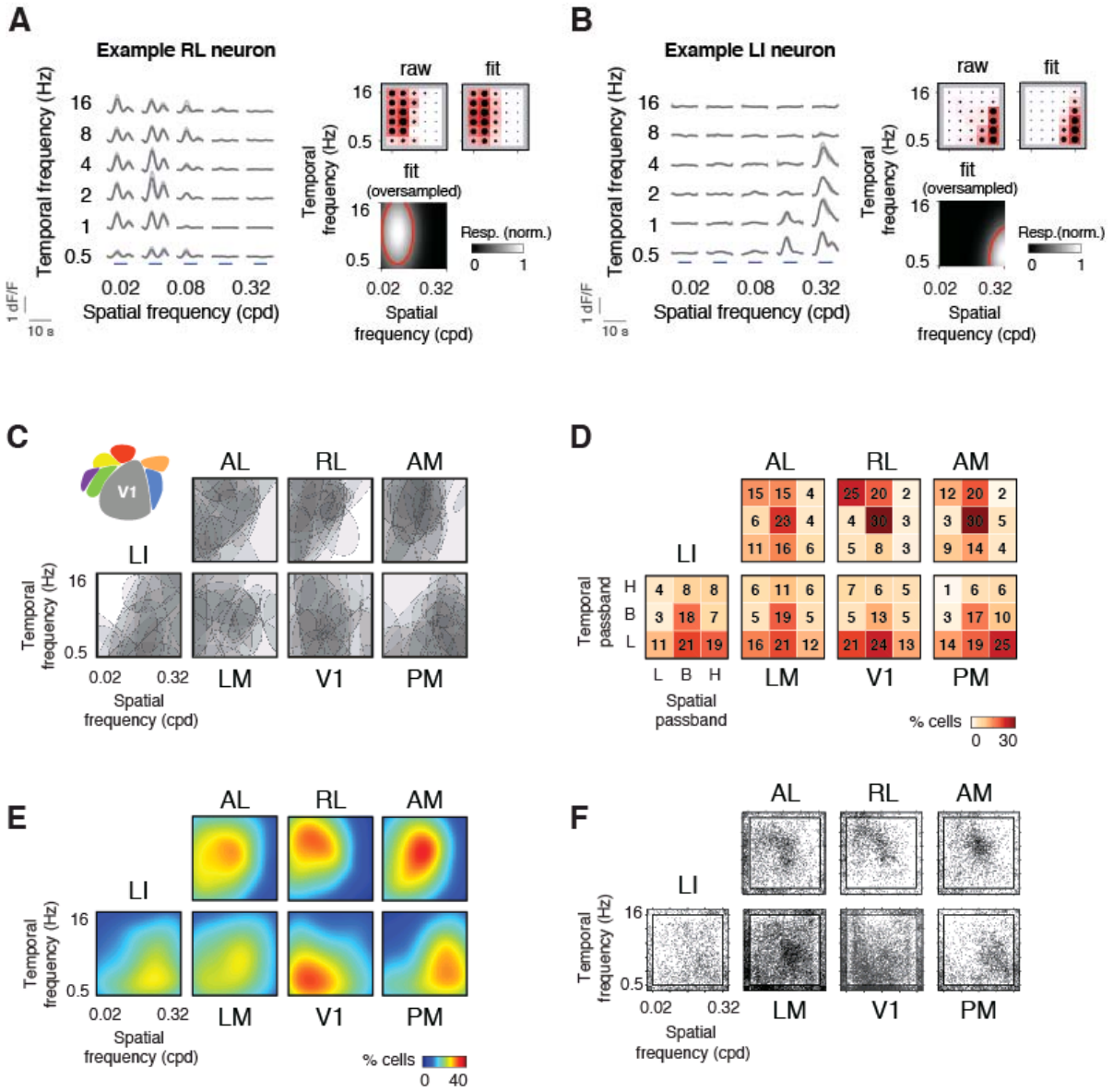

Figure 4. Segregated preferences for the spatiotemporal frequency across areas. (A) Example RL neuron selectively responding to low spatial frequencies and broadly tuned for temporal frequencies. Left panel: median responses across trials to different spatiotemporal frequencies. The average changes in fluorescence during the stimulus epoch are used to generate the response maps (right panel: raw), which are fitted to oriented two-dimensional Gaussian models (right panel: fit). Size of the dots and strength of red indicate the strength of response (normalize to range from 0 to 1). A high-resolution fit is generated by oversampling (right panel: fit-oversampled). Red line indicates the 50% peak response. (B) Same as A, an example LI neuron showing the selective response to low temporal and high spatial frequencies.

bioRxiv preprint doi: https://doi.org/10.1101/441014; this version posted October 12, 2018. The copyright holder for this preprint (which was not certified by peer review) is the author/funder. All rights reserved. No reuse allowed without permission.

(C) Superimposed surfaces showing diverse spatiotemporal tunings of 20 randomly selected cells. Inset: scheme of cortical areas. (D) Proportions of cell types based on the passband properties for spatial and temporal frequencies. H: highpass. B: bandpass. L: lowpass. (E) Proportion of neurons responsive to certain spatiotemporal frequencies across areas. (F) Scatter plots showing the distribution of preferred frequencies of the populations across areas. The inner box delineates the range of frequency explored in this study, dots at the boarders are scattered outward to visualize the distribution.

bioRxiv preprint doi: https://doi.org/10.1101/441014; this version posted October 12, 2018. The copyright holder for this preprint (which was not certified by peer review) is the author/funder. All rights reserved. No reuse allowed without permission.

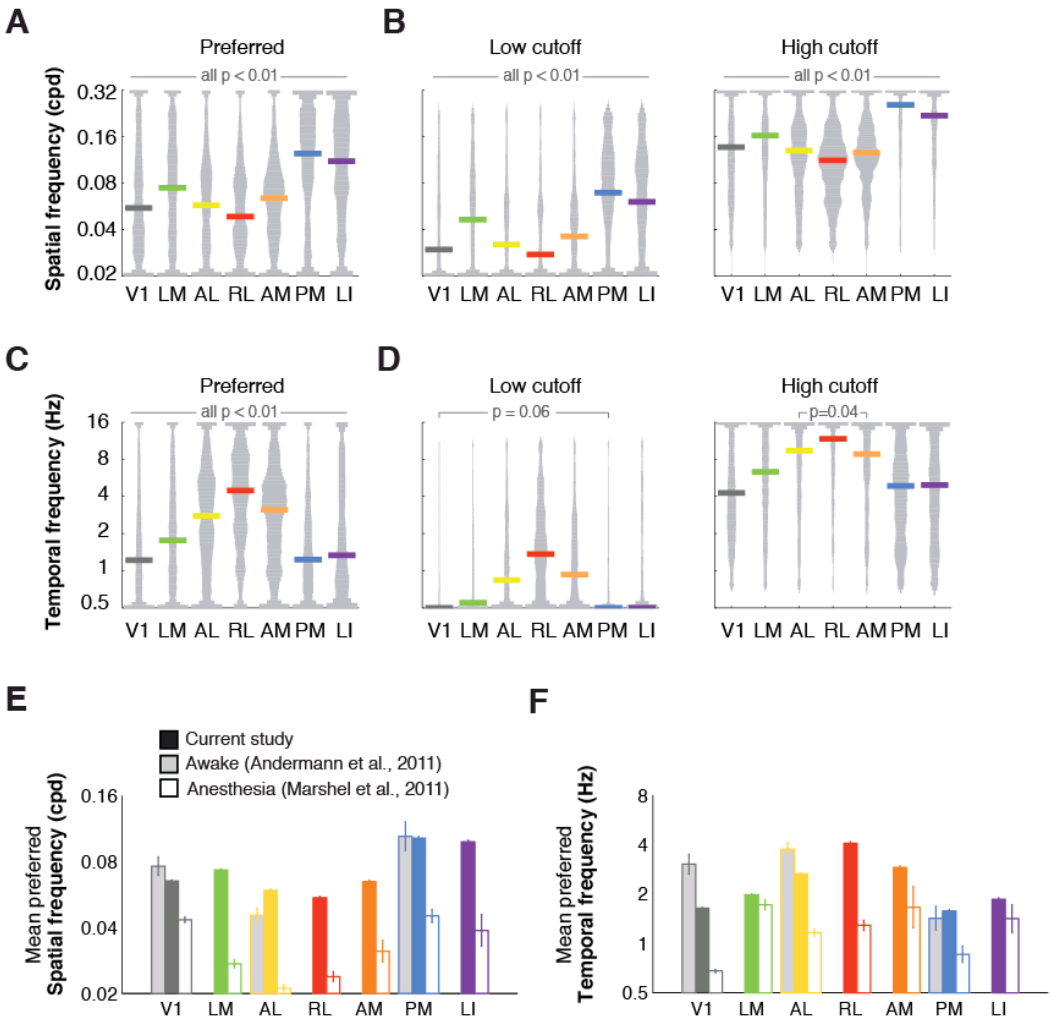

Figure 5: Spatiotemporal frequency selectivities: comparison to previous studies. (A) Distributions of the preferred spatial frequencies across areas. The width of each column is normalized to the maxima of the distribution. The median values are shown on top of each distribution as colored bars. (B) Distributions of low and high cutoff frequencies showing the range of frequencies represented by the populations in each area. (C-D) Temporal frequency analysis, same as (A-B). For all metrics (A-D), all distributions are significantly different from each other (KS tests with Bonferroni correction, $p<0.01$), except temporal frequency lower cutoffs in V1 versus PM ($p = 0.06$), temporal frequency high cutoffs in AL and AM ($p=0.04$). (E) Bar plots showing the comparison of mean preferred spatial frequencies across areas between this study and previous studies. Colored bars: the current study. Gray bars: awake mice (Andermann et al., 2011). Empty bars: anesthetized mice (Marshel et al., 2011). Error bars: standard error of the mean. (F) Comparison of mean preferred temporal frequencies across studies. Same as (E).

bioRxiv preprint doi: https://doi.org/10.1101/441014; this version posted October 12, 2018. The copyright holder for this preprint (which was not certified by peer review) is the author/funder. All rights reserved. No reuse allowed without permission.

The following figure supplements is available for figure 5:

Figure supplement 6: Spatiotemporal frequency analysis.

bioRxiv preprint doi: https://doi.org/10.1101/441014; this version posted October 12, 2018. The copyright holder for this preprint (which was not certified by peer review) is the author/funder. All rights reserved. No reuse allowed without permission.

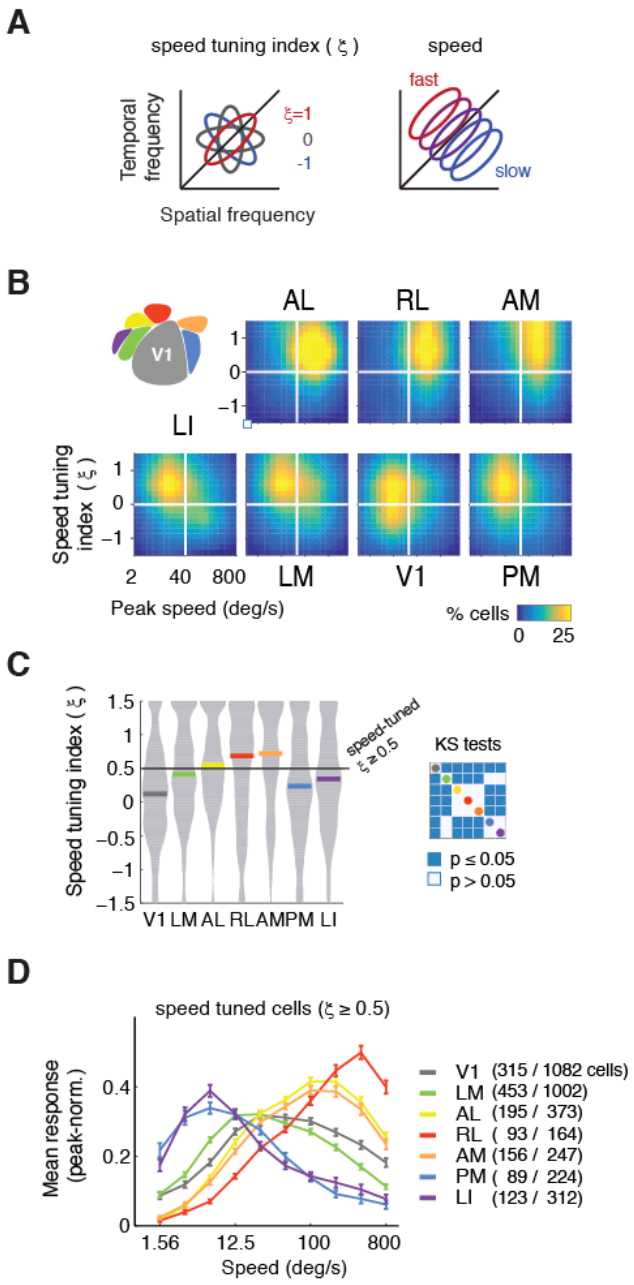

Figure 6: Complementary representation of visual motion speed in higher visual areas. (A) Schemes showing fits of different speed tuning indices ξ (left) and speeds (right). ξ ≈1, the neuron is speed tuned; ξ ≈0, untuned; ξ ≈-1, anti-speed tuned. The diagonals indicate iso-speed lines. (B) Heat maps showing different distributions of neurons across areas in the space of tuning index and peak speed. Inset: scheme of cortical areas. Higher area populations have higher tuning indices than V1, and encode distinct ranges of speed. (C) Distribution of speed tuning index ξ across areas. Colored bars show median values. Neurons above the threshold (ξ ≥ 0.5) are classified speed-tuned. The right panel shows the summary of the statistical

bioRxiv preprint doi: https://doi.org/10.1101/441014; this version posted October 12, 2018. The copyright holder for this preprint (which was not certified by peer review) is the author/funder. All rights reserved. No reuse allowed without permission.

comparisons across areas (KS tests with Bonferroni correction). (D) Population tuning curves for speed across areas. Each line is the average of peak-normalized speed tuning curves of speed-tuned cells within each area. Error bars: standard error of the mean. The numbers show the amount of speed-tuned cells in each population meet the criteria of speed-tuning analysis.

The following figure supplements is available for figure 6:

Figure supplement 7: Speed tuning analysis.

bioRxiv preprint doi: https://doi.org/10.1101/441014; this version posted October 12, 2018. The copyright holder for this preprint (which was not certified by peer review) is the author/funder. All rights reserved. No reuse allowed without permission.

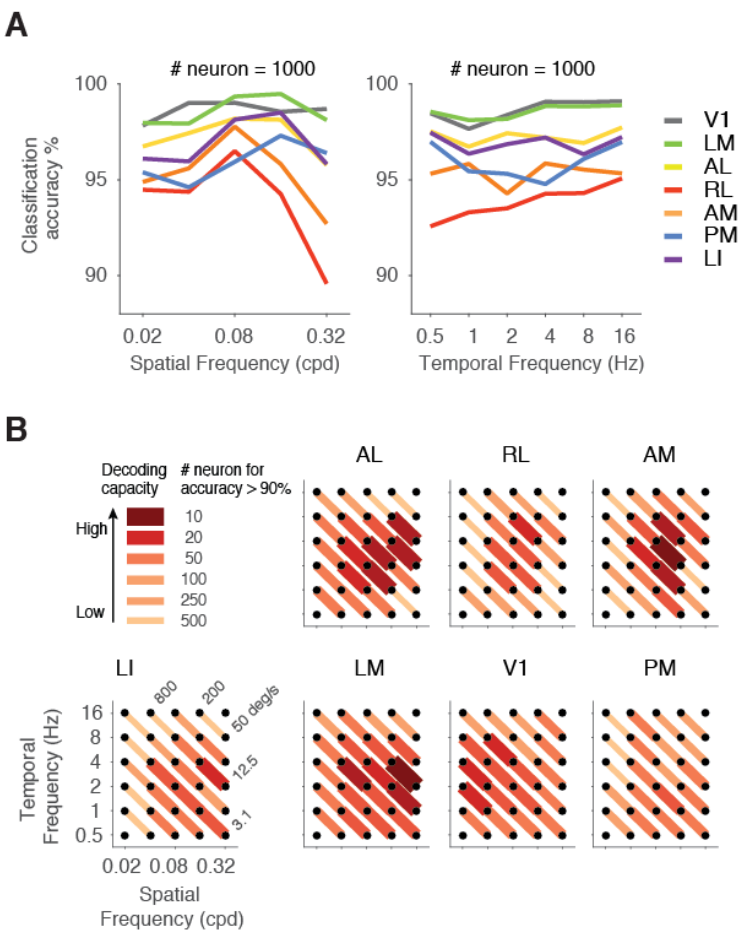

Figure 7: Enhanced speed discriminability in higher visual areas. (A) Stimulus classification accuracy at different spatial (left panel) and temporal frequencies (right panel) for individual randomly sampled populations (1000 neurons) per area. V1 and LM show nearly perfect performances across frequencies. Other higher visual areas show decreased performance. Error bars of each curve are ignored for visual clarity. Same plot with error bars can be found in Figure supplement 8D. (B) Speed discriminability at different spatiotemporal frequencies across areas. Higher visual areas show regional increases in performances comparing to V1. The red lines orthogonal to iso-speed lines show the decoding capacity for pairs of stimuli of 4-fold difference in speed. The redness and thickness indicate the magnitude of decoding capacity, which is the number of neurons needed for the accuracy > 90%.

The following figure supplements is available for figure 7:

Figure supplement 8: Population coding analysis.

bioRxiv preprint doi: https://doi.org/10.1101/441014; this version posted October 12, 2018. The copyright holder for this preprint (which was not certified by peer review) is the author/funder. All rights reserved. No reuse allowed without permission.

Supplementary figure captions

Figure supplement 1: Identification of visual areas. (A) Scheme of visual stimulation. A patch stimuli with a spectral noise background (0.08 cpd, 2Hz) continuously circles on the display along an elliptic trajectory. The phase of the trajectory is shown in color. (B) Phase map showing cortical regions responding to different phases of the trajectory. Each area has a representation of the full trajectory, resulting in a 'pinwheel' retinotopic map. (C) Sign map showing visual cortical areas (blue and red patches).

Figure supplement 2: Spectral noise stimuli. Spectral noise stimuli vary in three dimensions: spatial frequency (A), temporal frequency (C) and stimulus anisotropy (B). Isotropic noise stimuli (ISO) are generated by applying a bandpass filter with certain center spatiotemporal frequencies to random pink noises. Anisotropic noise stimuli (ANISO) have an additional narrow angular filter (bandwidth 5°), resulting in oriented stimuli. The stimuli rotated from 0 to 180 degree within each stimulus epoch to sweep the orientation space. Each stimulus set contains a combination of five spatial frequencies (0.02, 0.04, 0.08, 0.16, 0.32 cycle/degree) and six temporal frequencies (0.5, 1, 2, 4, 8, 16 Hz). In the stimulus anisotropy tuning experiment, orientation bandwidths are adjusted to generate stimuli with various stimulus patterns, from non-oriented to extremely oriented (360, 40, 10, 5°). (D) Description of the stimulus sets. (E) Scheme of the visual stimulation. Stimulus sets are presented as randomized sequences of 4s stimulus epochs, interleaved by 4s gray screen. Each of the 4 trials comprises a unique set of noise stimuli generated from a different seed. Hence the phase of stimulus contrast varies across trials, but the power remained constant.

Figure supplement 3: Higher visual area neurons have lower responsiveness and response reliability. (A) Example cells showing responses across trials with different responsiveness and variabilities. The top row for each cell shows the median responses across trials. The median absolute deviations across trials are shown as light gray shadow. Blue bars indicate 4s stimulus epochs. Gray scale bars indicate 1 dF/F and 10 second. The z-scored peak responses (z-score) and trial-to-trial correlation (corr.coef.) are noted above the time courses. (B) Cumulative distributions of z-scored peak responses of individual populations across areas. Cells with z-score values above 3 (peak response > 3x stand deviation of the baseline activity)

bioRxiv preprint doi: https://doi.org/10.1101/441014; this version posted October 12, 2018. The copyright holder for this preprint (which was not certified by peer review) is the author/funder. All rights reserved. No reuse allowed without permission.

are considered responsive. V1 shows higher responsiveness than higher visual areas. All pairs of areas are significantly different (KS tests with Bonferroni correction, all p values < 0.001). (C) Cumulative distributions of the trial-to-trial correlation of the populations across areas. Cells with correlation coefficient above 0.4 are considered reliable. V1 shows higher reliability than higher visual areas. All pairs are significantly distinct (KS tests with Bonferroni correction, all p values < 0.01). (D) Scatter plot showing the selection of responsive and reliable cells across areas. Reliably responsive cells are marked in red, the remaining population is shown in gray. Black lines indicate the thresholds.

Figure supplement 4: Clustering. (A) Scree plot showing the within-cluster sum-of-square as a function of number of clusters. There is no clear 'elbow' on the curve, suggesting a continuum of response types rather than discrete groups. Nevertheless, categorizing neurons into broad functional groups is useful for studying population response profiles across areas. The red cross marks the selection of 12 clusters, from where the increase in the cluster number lead to slower reduction of variance. (B) Bar graph showing average cosine distances between pairs of cells within clusters (blue) and between clusters (red). (C) Response matrix of 12 clusters across areas. Each row is the peak-normalized response profile of a single neuron. Black lines delineate the clusters. The stimulus conditions are annotated below the matrix.

Figure supplement 5: Summary of functional groups. (A) Distribution of individual clusters across areas. The dash line shows the fraction of one cluster if all 12 clusters are equally represented (1/12). (B) Heat maps showing the average of peak-normalized fits of the responses to ISO and ANISO stimuli. Clusters c1-8 prefer ISO stimuli, while c9-12 prefer ANISO stimuli. These clusters also present distinct spatiotemporal tuning properties. (C) Scatter plots showing the joint distribution of preferred frequencies. (D) Passband properties for the spatiotemporal frequency. (E) Average tuning curves for stimulus anisotropy, showing consistency with the preferences for ISO or ANISO stimuli in panel B.

Figure supplement 6: Spatiotemporal frequency analysis. (A) Spatial/temporal frequency analysis for the cell in Figure 4A. Left lower panel shows a high-resolution fit of the spatiotemporal response. The red contour shows 50% of the peak response. The tuning for spatial and temporal frequencies is measured as the cross sections at the preferred temporal and spatial frequencies respectively (gray dash lines). The spatial tuning profile is shown in the

bioRxiv preprint doi: https://doi.org/10.1101/441014; this version posted October 12, 2018. The copyright holder for this preprint (which was not certified by peer review) is the author/funder. All rights reserved. No reuse allowed without permission.

top panel. Low and high cutoff frequencies are placed at the half maxima, unless the cell responds to the upper or lower limits of the frequency spectra with over 50% of the peak amplitude. In this case, low cutoff frequencies are set at the lower limit, high cutoff frequencies at the higher limit. The bandwidth is measured at the half maxima in bandpass neurons. The right panel shows the temporal tuning profile, showing the highpass property of this neuron. (B) Same as A, for the cell in Figure 4B. (C) Proportions of highpass, bandpass, lowpass neurons (HP, BP, LP) for spatial frequencies across areas. (D) Distribution of spatial frequency bandwidth of bandpass cells. V1 population has higher median bandwidth than higher visual areas. RL has the narrowest bandwidth across areas. The width of the distributions is normalized to the maxima per area. Colored bars indicate median values. KS-test. (E-F) Same as (C-D), for temporal frequency.

Figure supplement 7: Speed tuning analysis. (A) Example neurons that are speed tuned (example AM cell) or untuned (example V1 cell). The speed tuning index ξ describes the interdependency between temporal frequency and spatial frequencies (also see Experimental procedures). If ξ close to 1, the cell is tuned for speed (upper left); if ξ close to 0, the cell has separable tuning for spatial and temporal frequencies (left panels; red and blue contours at 80 and 50% peak amplitude; white iso-speed lines with fixed ratios of temporal / spatial frequencies). (B) Speed-tune cells have similar tuning curves for speed at different spatial frequencies (upper middle), while the temporal frequency tuning curves change across spatial frequencies (upper right). Neurons with separable spatiotemporal tuning have similar tuning curves for temporal frequencies but not speed at different spatial frequencies (lower middle and right panels).

Figure supplement 8: Population coding analysis. (A) Classification accuracy for individual frequencies as a function of population size by visual areas. Each area presents different performances across spatial frequencies. The line colors correspond to the spatial frequencies. (B) Stimulus classification accuracy as a function of population size by visual area for all frequencies. V1 and LM outperform all other areas with all population size. RL shows the worst decoding performance among areas. Shaded areas represent standard errors. (C) Decoding capacity by area for individual frequencies. V1 and LM show outstanding decoding capacities for all frequencies. Other areas presented global decreases in performance with regional increase, which largely correspond to their preferred frequencies. The decoding capacity is defined as the number of neurons for accuracy above 90%. The dot size corresponds to the decoding accuracy. The intensity of the matrix shows the min-max scaled decoding capacity per

bioRxiv preprint doi: https://doi.org/10.1101/441014; this version posted October 12, 2018. The copyright holder for this preprint (which was not certified by peer review) is the author/funder. All rights reserved. No reuse allowed without permission.

area. (D) Stimulus classification accuracy at different spatial (left panel) and temporal frequencies (right panel) for individual randomly sampled populations (1000 neurons) per area. V1 and LM show nearly perfect performance across frequencies. Other higher visual areas show decreased performance. Same as Figure 7A, but with error bars (shaded areas, standard error of the mean). (E) Decoding for iso-speed pairs at different spatiotemporal frequencies across areas. Each areas showed regional enhancements of the decoding performance. The red lines connect iso-speed pairs. The redness and thickness indicate the magnitude of decoding capacity, which is the number of neurons needed for the accuracy > 90%.